Target Classification and Remote Sensing of Ocean Current Shear Using a Dual-Use Multifrequency HF Radar

Dennis Trizna, *Senior Member, IEEE*, and Lillian (Xialon) Xu

***Abstract*—In this paper, we describe a high-frequency (HF) radar capable of multifrequency operation over the HF band for dual-use application to ship classification and mapping ocean current shear and vector winds. The radar is based on a digital transceiver peripheral component interconnect (PCI) card family that supports antenna arrays of four to 32 elements with a single computer, with larger arrays possible using multiple computers and receiver cards. The radar makes use of broadband loop antennas for receive elements, and a number of different possibilities for transmit antennas, depending on the operating bandwidth desired. An option exists in the choice of monostatic or multistatic operation, the latter providing the ability to use several transmit sites, with all radar echo signal reception and processing conducted at a single master receiver site. As applications for such a multifrequency radar capability, we show measurement and modeling examples of multiple frequency HF radar cross section (RCS) of ships as an approach to ship target classification. Results of using 32 radar frequencies to measure the fine structure in ocean current vertical shear are also shown, providing evidence of one edge of a 1–3-m deep uniform flow masked at the surface by wind-driven current shear in a different direction. Other applications of current-shear measurements, such as vector wind mapping and volumetric current estimation in coastal waters, are also discussed.**

***Index Terms*—High-frequency (HF) radar, ocean currents, remote sensing, target classification.**

I. Introduction

ORIGINALLY, high-frequency (HF) radar technology in the United States was developed for classified military applications under defense funding, for aircraft and ship tracking at long range using the ionosphere to achieve long-range propagation (see, for example, [1] and [2]). The refractive properties of the ionosphere in the 3–30-MHz range were utilized as an effective overhead mirror, reflecting radar energy transmitted at angles above the horizon, to extend propagation over the horizon and achieve radar coverage to thousands of miles. Due to the requirements of adapting to the changing diurnal properties of the ionosphere, multifrequency capability over a modest range of frequencies was required to maintain coverage of an area over a 24-h period. Research using a modest band of frequencies was conducted through the 1960s and 1970s at the U.S. Naval Research Laboratory (NRL), Washington, DC [3], [4] and the Stanford Research Institute (SRI), Stanford, CA [5]–[7] as proof of principle of the potential for skywave over-the-horizon (OTH) radar, most of it classified. As an outgrowth of that research, an example of a high-level example in frequency diversity was developed jointly by the United States and United Kingdom and sited at Orfordness, East Anglia, England, for Cold War surveillance applications.[1] This radar system used a series of adjacent log-periodic antennas to cover the 6–40-MHz band, and required several hundred acres of near-coastal land area for the antenna array. The surface wave mode of operation on the other hand takes advantage of the highly conductive sea surface in the HF band, and depends on focussing the transmitted energy density at grazing angles toward the horizon. The sea surface acts as an electromagnetic waveguide in a sense, and radar energy can also propagate behind the horizon using this mode of propagation. Again, more details may be found in [1] and [2].

The earliest surface wave multifrequency work produced results using multifrequency HF radar data to demonstrate that current shear could be measured using such systems [8]. Teague [9] and later Fernandez *et al.* [10] utilized multifrequency radars to demonstrate the measurement of current shear in the ocean.

Additional multifrequency work under a jointly operated National Oceanic and Atmospheric Administration (NOAA)/U.S. Navy radar at San Clemente Island, off the California coast, made measurements of directional wave spectrum [11]. These results demonstrated the wave-frequency-dependent azimuthal spreading characteristics predicted by the Phillips resonance mechanism. While attempts were made to promote OTH skywave radar for remote sensing to the U.S. Navy in the 1970s, the promise of oncoming satellite-based synthetic aperture radar for global ocean wave measurement prevented acceptance by the U.S. Navy of the OTH radar remote sensing concept. As a result, remote sensing research in this area at NRL ceased in the early 1980s. However, work in this area continued on several fronts, including the use of the U.S. Navy relocatable-over-the-horizon-radar (ROTHR) system in later years [12], [13]. Utilization of a single frequency using surface wave propagation was developed in the 1970s for remote sensing of ocean currents. Today, it provides a robust tool for mapping currents for ocean modeling and ocean current studies, offering the oceanographer for the first time extensive area coverage heretofore unattainable [14], [15]. The application of current-shear mapping using four radar frequencies has been demonstrated as a reliable measure of near-surface current shear using comparisons with *in situ* current sensors [16], and has been recently used to estimate surface wind fields [17].

Manuscript received December 1, 2004; accepted July 17, 2006. This work was supported in part by the U.S. Office of Naval Research, Surveillance Division, under Contract N00014-03-C-0197. **Associate Editor: L. R. Wyatt**.

The authors are with the Imaging Science Research, Inc., Burke, VA 22015 USA (e-mail: dennis@isr-sensing.com).

Digital Object Identifier 10.1109/JOE.2006.886198

[1] http://www.cufon.org/cufon/cobramst.htm

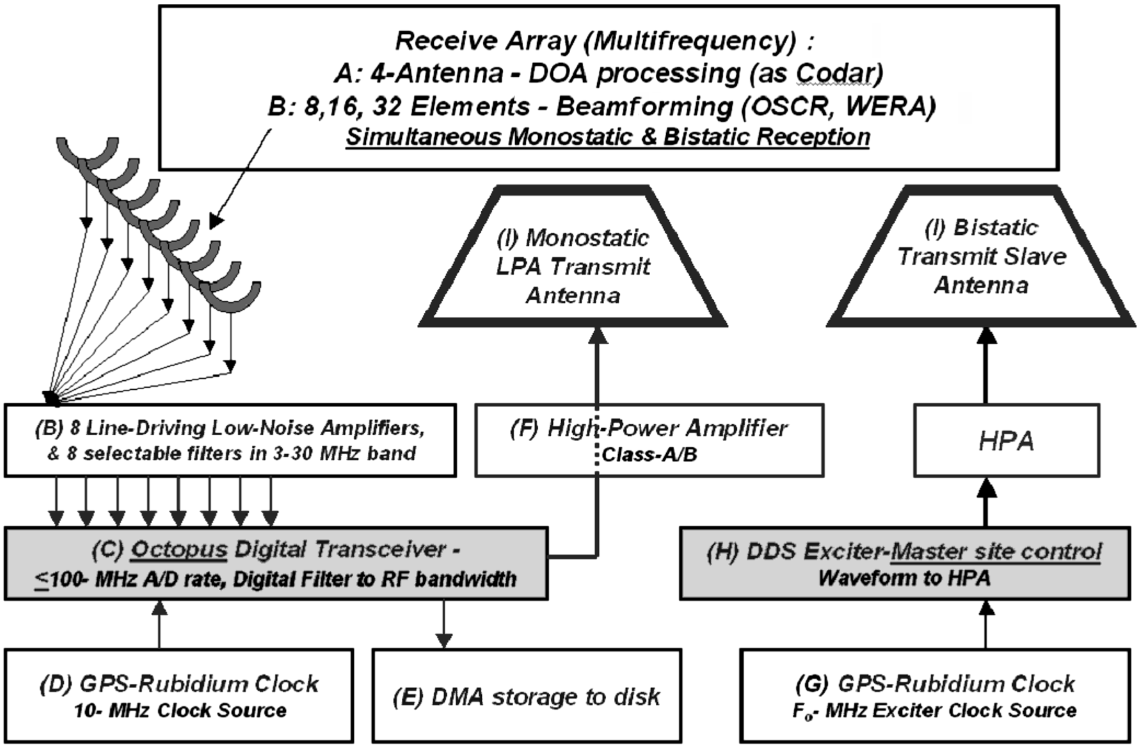

Fig. 1. Basic layout of the ISR HF radar system, showing a bistatic transmit site on the right, and a master transmit–receive site on the left that also acts as a monostatic radar, simultaneously receiving echoes from both transmitter sites.

In this latter application, current shear and direction agree well with the onshore–offshore directions and magnitudes associated with the sea-breeze effect.

The attainment of a commercial radar to obtain multifrequency measurements has up until now been difficult and expensive due to the complexity of building radar receivers using multiple-frequency switching and radio-frequency (RF) components. To overcome this obstacle, we have developed a purely digital transmit–receive system to serve as the basis of a multifrequency radar, which promises to improve the reliability and lower the costs of production of such a system. Of course, due to the wideband nature of the remaining components, namely the transmit and receive antennas, the complexity and space requirements for such a radar grow to a degree relative to compact colocated antenna systems, but without a major corresponding increase in cost. The results of these radar developments are described in this paper, along with some examples of their application.

II. Radar System Design

The radar layout schematic for the multifrequency system is shown in Fig. 1, with an arrangement of bistatic and monostatic transmit and receive sites shown. A pair of monostatic radars is also an option. For the bistatic geometry, rubidium clocks are necessary to keep accurate time and frequency stability, as the master clocks of the transmit and receive sites must be effectively phase-locked to provide the dynamic range necessary for good quality Doppler spectra. At the heart of either option is the Imaging Science Research (ISR), Burke, VA, eight-channel digital transceiver, the Octopus, which includes a global positioning system (GPS) receiver on board to provide timing for the bistatic operation, or to allow two monostatic radars to share radar time slots while operating at the same frequency. The transceiver transmits a fully programmable waveform [simple pulse, frequency-modulated pulse, or frequency-modulated continuous wave (FMCW)] that is cabled to a high-power amplifier (HPA), and then fed to a transmit antenna. This can be a single monopole, a two- or four-element monopole array with modest azimuthal directivity, or a broadband log periodic array to cover the 3–30-MHz HF band for continuous multifrequency operation. This will be described in more detail in the following paragraphs.

A. Transmit Antenna

A new radar antenna was designed for continuous coverage over the entire 3–30-MHz band, a modified log-periodic array (LPA) antenna. This is shown in Fig. 2 deployed at the U.S. Army Corps of Engineers (USACE) Field Research Facility (FRF) test site in Duck, NC, and extends roughly 15 m in the cross shore direction. However, more compact designs are feasible for operation at prespecified selected frequencies of four or eight say for current-shear measurement. These include two- and four-element square arrays that provide directivity toward the sea, as well as a simple monopole which is omnidirectional. The LPA antenna provides full tunability to any frequency in the HF band, and is appropriate for target classification ship radar cross section (RCS) measurement applications.

B. Receive Antenna Array

The radar echo is received on a multielement antenna array, 4–32 elements, depending on requirements of the application. Ocean current sensing typically will utilize a four-element array,

Fig. 2. Four-loop element receive array and a log-periodic monopole transmit antenna for 3–30-MHz tunability are shown at the HF radar test facility located at the USACE FRF field site.

as shown in Fig. 2, where elements are spaced 8 m apart. With the first element just 4 m from the transmit array, a length of coastline less than 30 m is sufficient for deployment. Sea spectrum measurements and target tracking and classification applications will utilize a 16- or 32-element array to obtain high azimuthal resolution. For ocean current sensing, this assures a measurement at each azimuth in incremental fashion, typically at half-beamwidth steps. Direction-of-arrival methods of current measurement quite often have azimuthal gaps in coverage, and azimuthal interpolation is required to fill in the azimuthal coverage. For target classification, a large array assures a good signal-to-noise for weak target echoes. For single-frequency radars, simple monopole antennas are used for the array. For broadband frequency designs operating over several radar frequencies across the HF band, loop antenna elements are used. The units currently used were originally developed at the University of Michigan, Ann Arbor, and similar units are currently in operation at the Long Marine Laboratory, Santa Cruz, CA. However, we have added an improved ISR-designed preamplifier within the loop antenna that has a 3–30-MHz filter imbedded to eliminate amplitude modulation (AM) and frequency modulation (FM) interference, plus constant impedance across the HF band.

C. Signal Conditioning Chassis

The received echo signal is then cabled to a signal conditioning chassis (SCC) [item (B) of Fig. 1] that serves two purposes. First, it provides a direct current (dc) power to the loop antenna preamplifiers when these are used. Second, it can have installed switchable narrowband filters to eliminate other user signals in the HF band, to increase the sensitivity settings on the transceiver card input line. Each SCC can have up to eight frequency filters for each of eight receiver channels that are switched pulse-to-pulse as the radar frequencies are sequenced. For systems that require more than eight frequencies, these boxes can be combined in line, each with its own address, to provide multiples of eight frequencies. For more than eight element arrays, these units are installed in parallel. For existing applications, the radar is operated with only the 3–30-MHz front–end filter in the loop. The possible recorded data dynamic range of 9–16 bit (if one sums 2 to 256 waveforms on the board before transfer) that is achieved typically is sufficient to handle the largest ambient user signals in the HF band. For the case of a single local strong interfering signal due to nearby transmitters, one can add a single narrowband inline filter to avoid the necessity of the switching filters in the SCC. The switching filter option in the SCC is recommended for use in target detection applications, when optimal dynamic range is desired. For current sensing applications, the Bragg lines are typically the largest echoes in the Doppler spectrum, and the switching filters can be eliminated, saving in SCC cost.

D. Octopus Transceiver

The eight-channel transceiver card, the *Octopus*, is a self-contained radar digital engine on a single peripheral component interconnect (PCI) card, with a pair of phase-locked direct digital synthesizer (DDS) chips, two field-programmable gate arrays (FPGA), a pair of four-channel digital down converters (DDC), and eight receive analog-to-digital (A/D) channels. For arrays of more than eight elements, a scaled-down receive-only Octopus is available, called the *OctRec*, and three of these cards can be installed on the same computer with an *Octopus* to allow reception of 32 channels. For arrays larger than 32, additional computers are recommended to house groups of four OctRec cards, with trigger and A/D clock timing provided by the master receive transceiver using external cable connections from one unit to the next. The transceiver card has several features, which are discussed next.

1) GPS Receiver Time Lock: A GPS receiver is imbedded in the board and all of its capabilities can be utilized. The one pulse-per-second (1-PPS) time tick from the GPS unit is the industry standard to phase-lock oscillator clocks to a long-term stable frequency as well as standard time. The system clock can be an onboard oscillator, or an external ISR rubidium clock, that is also capable of being locked to GPS time. The latter is recommended for bistatic systems, where precise timing and frequency control and good phase noise characteristics are required. Such phase noise in typical oscillators occurs due to short-term frequency drift between two crystal oscillators, and its suppression is more important for high dynamic range applications, where small RCS target detection is required in the presence of strong Bragg-line echoes. Alternatively, high-frequency stability is needed to avoid the interpretation of a slight difference in transmitted frequency between the two transmit sites as a surface current induced Doppler shift. We have demonstrated long-term stability over 2-h periods of less than 2-mHz difference in frequency between two ISR rubidium clocks, amounting to a few centimeters per second ocean radial current error.

2) External Chassis Control: The *Octopus* transceiver has a serial connector for control of exterior devices, such as the SCC described previously. Filters are switched with each trigger using this external chassis control (ECC) connection. Other devices can also be controlled, and these will be available as an option in the future.

3) Transmit–Receive Section: Two DDSs that are phase-locked are utilized, one to generate the transmit pulse and the second to generate the clocking samples for the A/D converters that must be phase-locked to the transmitted phase. The transmit DDS-1 can be programmed for simple pulse or frequency-modulated pulse operation that allows pulse compression and higher effective peak power. The user has full use of envelope control, allowing a rectangular, a triangular, a cosine-squared, or a user-defined envelope. The envelope is digitally synthesized, passed through a D/A converter, then to an RF mixer on the card where it is mixed with the rectangular envelope RF signal of DDS-1. One can choose either to 1) use input channels to record array antenna input signals in pairs of 2, 4, 6, or 8 elements, or 2) to record the DDS-1 and the mixer outputs directly on the board (channels 1 and 2, respectively), for pulse compression application or for testing. The other remaining channels then are used to simultaneously record other antenna inputs. Combinations of 20-dB gain plus 0-, 6-, or 12-dB attenuation are available on the board to fit the input signal to the optimal A/D input levels of 1 V, peak-to-peak. Preamplification is also present on the loop antenna elements.

4) A/D Conversion and Two- Stage Digital Filtering: The transceiver makes use of low power ($\sim$1/4 W) 8-bit A/D converters that run at a maximum of 100 MHz, which allows placement of eight such channels on the board. Faster rates or higher bit A/D chips typically run too hot to allow eight chips on a single card, so higher dynamic range is achieved for recording by one of two methods. The first is the use of DDCs on the board to apply linear filtering, producing in-phase and quadrature (I/Q) samples pairs with dynamic range improvement equal to the ratio of the sample rate divided by the filter bandwidth, but is not fully implemented at this time. The board also utilizes onboard first-in–first-out registers (FIFOs) to sum up to 256 consecutive echoes for each channel, creating a 16-bit word before writing off to a storage disk file. For example, operating at a single frequency at a trigger pulse repetition frequency (PRF) rate of 1024 Hz, and summing 256 consecutive pulses, one achieves a 16-bit output at a 4-Hz recording rate. Using two transmitted radar frequencies, one can either use 256 sums for a 2-Hz rate per frequency, or a sum of just 128 pulse echoes to maintain the 4-Hz recording rate. A doubling of radar frequencies requires halving the number of waveforms summed, trading one effective bit stored for each doubling of the number of radar frequencies. The DDS-1 transmits the same radar frequency for the number of waveforms to be summed before shifting to the next in the sequence. For a case of 32 radar frequencies used for ship RCS measurements that we have conducted, just 16 pulses were summed, maintaining a 2-Hz recording PRF with 12-bit data accuracy. The output data are always stored in 2 B per data point, even if choosing not to sum. Offline, the data are digitally filtered in software. For typical HF radar applications, we digitize at a 60-MHz rate, resulting in offline digitally filtered data at the PRF rate, I and Q, with additional gain as a result of this digital filtering process. For a pulse length of 8.5 μs, ($\sim$512 samples at 60 MHz), one would choose a 512-point filter to match the pulse length, resulting in an additional 27 dB of processing gain. For this case, the data that are submitted to Doppler processing are I/Q samples with 25-bit accuracy. Doppler processing then provides additional gain. For a 2-Hz final PRF and coherent integration time of 512 s, an additional 30-dB processing gain is achieved. For this example, the Doppler spectrum has a dynamic range of 105 dB.

E. Linux Operating System

A Linux operating system was chosen for its efficient bus transfer of data at high speed from the transceiver card. To minimize errors in data transfer, only the acquisition user program is run during data collection, and no other user processes are allowed other than those associated with acquisition. After a collection, the data are automatically transferred to a networked Windows machine for storage, Doppler processing, and analysis. Currently, the first stage of digital processing is done in software at this time, as the data are recorded at 60-MHz sampling rate. Work is currently underway to make use of the onboard DDC filtering, which will allow I/Q sampling output commensurate with the bandwidth of the transmitted signal as described earlier, and reduce the data transfer rates and volume of data recorded.

F. High-Power Amplifier

The high-power amplifier is built in house, for programmability using our ECC option, and provides a peak power of 500 W per unit. Typical average power for operation is of the

TABLE I
RADAR PARAMETER EXAMPLES AND MAXIMUM RANGE COVERAGE USING 16 FREQUENCIES AND A 60-MHz SAMPLE RATE. HALVING THE NUMBER OF FREQUENCIES DOUBLES THE MAXIMUM RANGE COVERAGE

Radar acqisition parameters:						
# samples	*# freqencies*	*PRF (Hz)*	*Sample Sum on FPGA*	*PRF/frequency (Hz)*	*Data Rate (MB/s)*	*Range Extent (km)*
8192	16	1024	32	2	2.048	20.48
16384	16	1024	32	2	4.096	40.96
24576	16	1024	32	2	6.144	61.44

order of 5 W for a 10-μs pulse (1.5-km range resolution); 50 W using frequency-modulated chirp pulsing with a 10-1 compression ratio and a 100-μs FM chirped pulse at a 1-kHz PRF; or the full 500 W if FMCW operation is used. To date, the simple pulse has been used, and FM chirp is currently being tested.

G. Rubidium Clock Option

The rubidium clock integrated option is assembled in house, using a Stanford Research rubidium unit, and is suggested for target detection and classification applications, where dynamic range of the order of 100 dB may be required for small target cross sections.

H. System Capabilities

The initial thrust of development of the radar system has been in support of short-range naval ship measurements using 32-frequency operation on a pulse-to-pulse basis. Because of the short range to target requirement, simple pulses were used for this application, typically 10 μs, providing 1.5-km range resolution. Range coverage capabilities have not been established using such data, as the large number of frequencies forced a relatively short-range coverage of just 20.5 km maximum using a 60-MHz A/D conversion rate and 8192 samples. The data throughput has satisfied the expected capability of 64-MB/s burst rate and ~6-MB/s maximum mean rate using the 32-bit personal computer (PC) bus. Using a pulse repetition frequency of 1024 Hz, with 32 frequencies, summing 16 2-B samples on the board before direct-memory-access (DMA) transfer, a 2-Hz PRF per frequency results. The mean throughput rate with such a combination is then limited to 2.05 MB/s and a range extent of 20.5 km. The maximum mean rate of ~6 MB/s forced by the bus speed and DMA transfer will allow three times the number of samples and range extent of 61.5 km. Maximum dynamic range capability can be improved with the 2-Hz PRF/frequency by increasing the number of samples summed on the transceiver at the expense of the number of frequencies or range samples. Examples of different combinations of parameters and maximum range extent are given in Table I, based on the maximum throughput of 6 MB/s and a 60-MHz digital sampling rate that covers the 3–30-MHz HF band.

Tests are now underway that utilize frequency-modulated pulses for ocean current measurements at long range using fewer frequencies. Pulse compression of 10–1 will be tested first using 100-μs transmit pulse lengths, compressed to 10-μs length. These correspond to a minimum range of 15 km and 1.5-km range resolution. Duty cycles of as much as 50% are possible, at the expense of a longer minimum range.

III. TARGET CLASSIFICATION

A. Small Boat RCS versus Radar Frequency

Experiments conducted in the 1970s by an NRL Radar Division group that included the first author of this paper demonstrated that ship and small boat targets have a RCS "spectroscopic fingerprint," i.e., a unique template of RCS versus radar frequency across the 3–30-MHz HF band. Fig. 3 shows an example of data from a report [18] using a commercial fishing boat target. The experiments were an attempt to assess the potential for using HF radar to detect small fishing and pleasure craft for range safety applications to missile test ranges of the west coast of the United States, an application that was never implemented. The results were not classified, but at the time were not considered sufficiently significant for publication. However, they now provide an interesting example of a potential small boat classification method using multifrequency HF radar. In addition to the bulkhead, the other metal structures on the boat were the mast and fishing leader lines hanging vertically from the stowed fishing gear which could act as vertical monopole scattering elements. The mast was the tallest element at 16.6 m high, corresponding to a quarter wavelength monopole resonant radar frequency, F_R, equal to 4.5 MHz. Over a perfect ground plane that the ocean surface presents at HF, an electrical image is generated so that the mast behaves as a dipole in free space. Fig. 4 shows a plot of the RCS of a monopole 7.5 m high. The low-frequency behavior rises as F_R^8, in the so-called Rayleigh region. At higher frequency, the RCS falls as F_R^{-2}, with additional peaks at odd integer times one quarter wavelength. For longer length monopoles, the RCS rises with the F_R^{-2} asymptote.

Other scattering elements, such as the cabin and fishing lines described previously, will contribute to the RCS in a complicated fashion that depends upon the spacing of each possible element. For this case, the fishing leader lines were positioned on either side of the boat, and with the mast were aligned at the corners of an equilateral triangle. As this lateral spacing is not known, we do not attempt to model this specific target, but an example of the behavior of a two-element target provides an interesting comparison that illustrates the radar-frequency dependence of multielement targets. Moreover, as our interests lie in bistatic illumination as an additional dimension for classification, this feature is demonstrated in the following section.

B. Bistatic RCS Model Using Monopole Elements

Fig. 5 shows the geometry for a bistatic scattering condition for two monopoles spaced by a distance L seen in plan view from above. Each has a respective scattering cross section σ_1 and

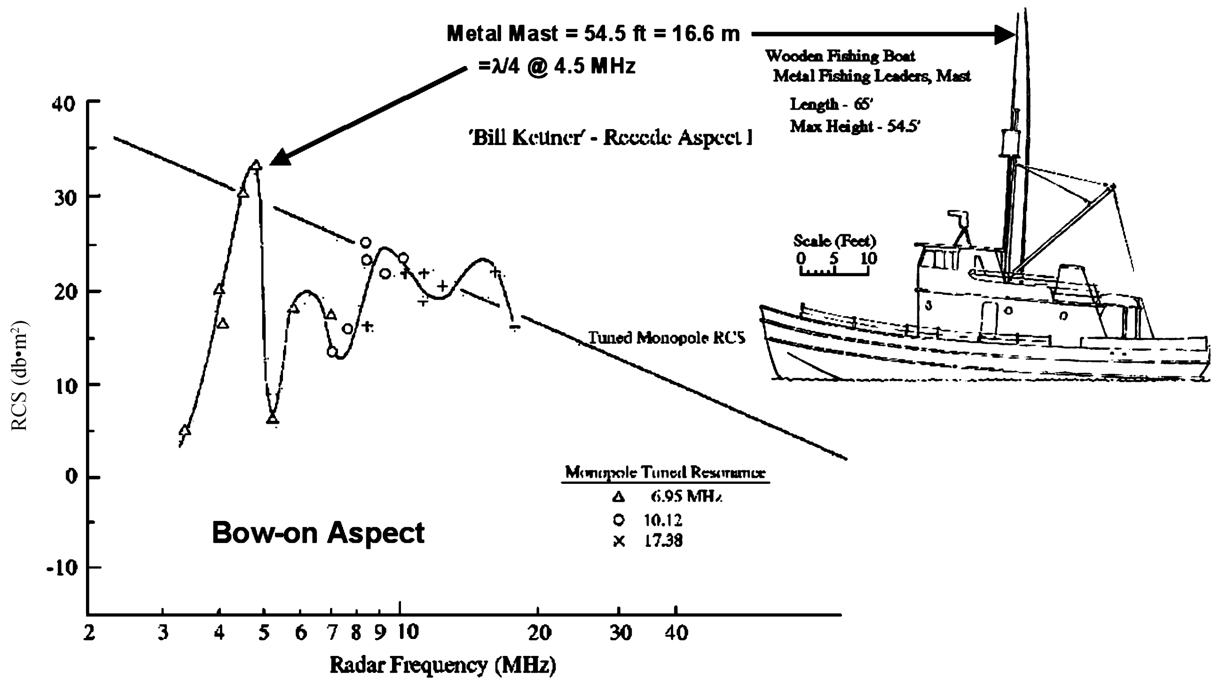

Fig. 3. RCS versus frequency for a fishing boat is dominated by the quarter wavelength monopole contribution of the metal mast, showing a peak at the resonant frequency.

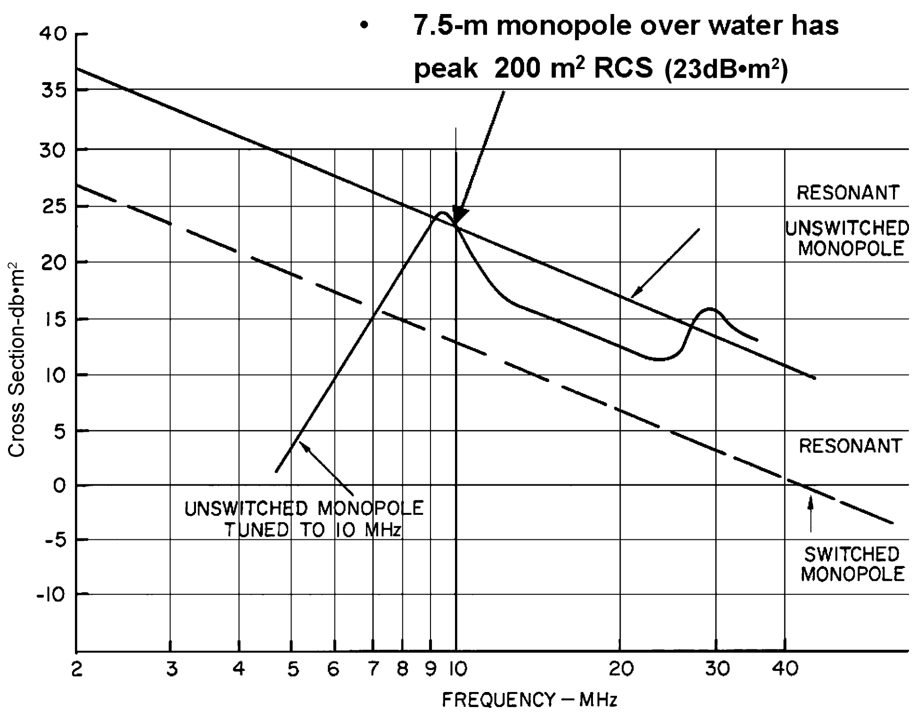

Fig. 4. RCS as a function of frequency for a 10-MHz resonant monopole.

σ_2, and each is a function of radar frequency. The illuminator generates a surface mode plane wave along a propagation direction separated from the scattered direction to the receive array by bistatic angle Φ_B. The aspect of the target's course heading relative to the receive array is Φ_A. Since the monopole RCS is omnidirectional, the scattered fields from the two elements will sum with a phase difference $k(L_1 + L_2)$, where k is the radar wave number, $\lambda/2\pi$. From Fig. 5, the phase path difference for scatter from the pair of monopole scattering elements, along the bistatic scattering paths shown, is simply the sum of

$$L_1 + L_2 = L\cos(\Phi_B - \Phi_A) + L\cos(\Phi_A). \quad (1)$$

The radar equation for scatter from a single target can be written as a ratio of received power P_R, to transmit power P_T [19]

$$P_R/P_T = G_T G_R \lambda^2 \sigma / [(4\pi)^3 R_1^2 R_2^2 l_1 l_2] \quad (2)$$

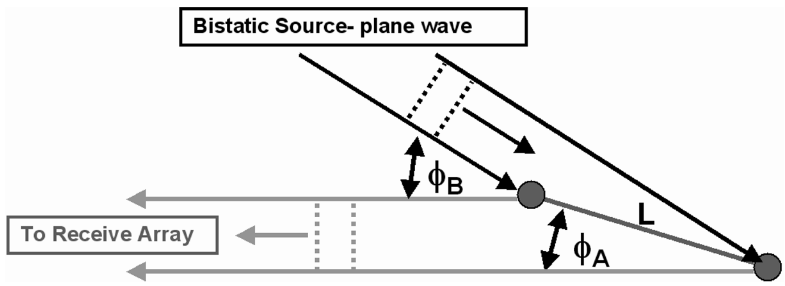

Fig. 5. Bistatic scattering geometry for source at top and receive array to left, with bistatic angle Φ_B and target aspect angle relative to receive array Φ_A.

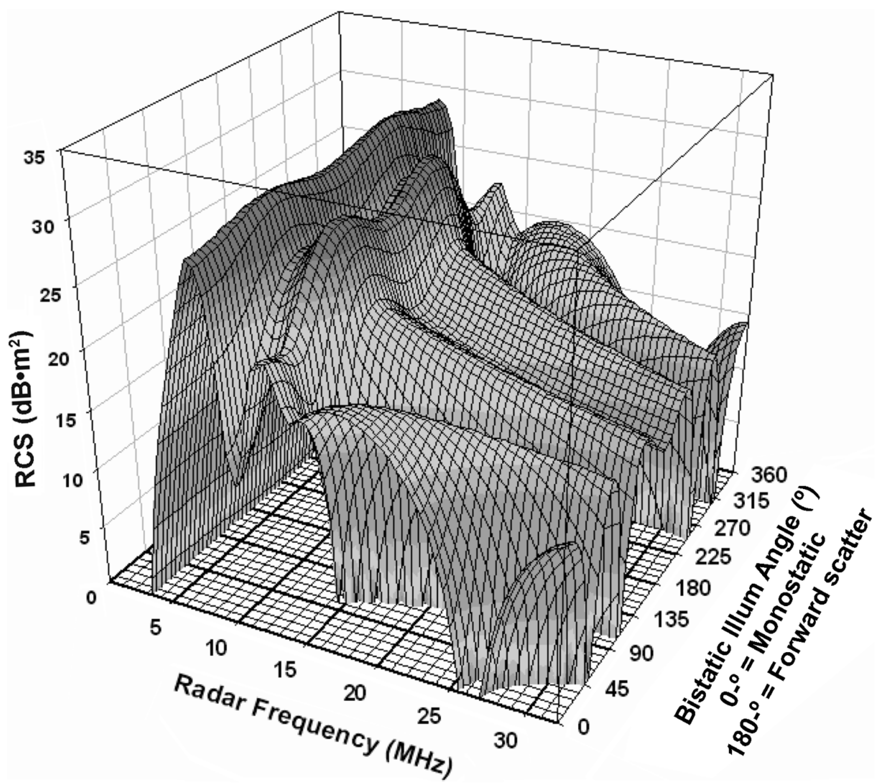

Fig. 6. Bistatic RCS of a pair monopoles spaced by 5 m over a perfect ground screen, resonant at 6 and 12 MHz. Variation is versus frequency and bistatic angle for a fixed heading 0° to the receive site.

where subscripts T and R refer to transmit and receive elements, λ is the radar wavelength, σ is the RCS, R_1 and R_2 are the distances from the transmitter to the target, and target to receiver, respectively, and l_1 and l_2 represent propagation losses over the same paths. The field strength ratio from a single target is proportional to the square root of (2), and will have a phase given by $\exp(ikx)$, where $x = R_1 + R_2$. For scatter from two elements separated by distance L, as shown in Fig. 5, with L much less than either L_1 or L_1, so that $R_i + L \sim R_i$, then the summed scattered fields E_{SUM} can be written as

$$E_{\text{SUM}}/E_T = \left[G_T G_R \lambda^2 \big/ \left((4\pi)^3 R_1^2 R_2^2 l_1 l_2\right)\right]^{1/2} \times \Big[(\sigma_1)^{1/2} \exp\{ikx\} + (\sigma_2)^{1/2} \exp\{ik[x + L\cos(\Phi_B - \Phi_A) + L\cos(\Phi_A)]\}\Big]. \tag{3}$$

The total RCS σ_T is calculated by taking the product of (3) times its complex conjugate, rearranging terms to give

$$P_R/P_T \sim \sigma_T = \sigma_1 + \sigma_2 + [(\sigma_1)^{1/2}(\sigma_2)^{1/2}] \times \cos\{k[L\cos\Phi_A, +L\cos(\Phi_B - \Phi_A,)]\}. \tag{4}$$

A simple two-mast model based on monopoles resonant at 8 and 12 MHz and spaced 7.5 m apart was used to generate the bistatic received power as a function of bistatic angle. The data of Fig. 4 was taken and scaled to arbitrary resonant frequency, producing appropriate frequency-dependent RCS contributions. For bistatic illumination, the aspect angle (ships course relative to direction to receive antenna) introduces an additional variable and is taken to be zero for this example. The bistatic RCS calculated from (4) for this combination and spacing is shown in Fig. 6. The monostatic result occurs at 0°, and looks similar to the earlier data for the fishing boat, but with just two primary resonances now. The higher odd-quarter wavelength resonances also appear at higher frequency. As the bistatic illumi-

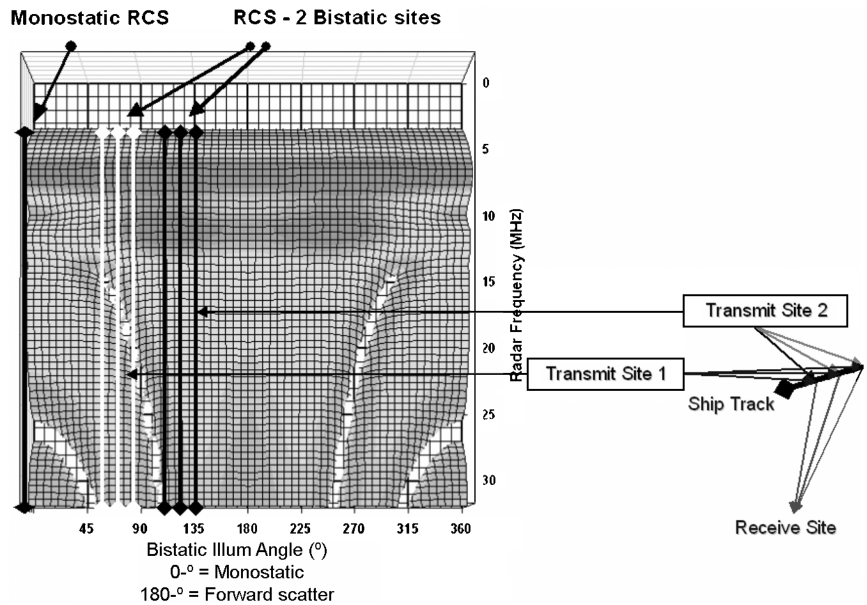

Fig. 7. RCS plan view with bistatic geometries shown for three locations of ship along course, each of which results in three different azimuthal angle results for each bistatic transmitter. The monostatic result is fixed assuming negligible change in aspect along course.

nation angle changes from monostatic, the relative path length between the two elements changes according to (1). A number of peaks and nulls in RCS are very distinctive and could serve as a dual-mast ship target classification signatures. For more complicated ship superstructures, similar methods could be used be used to generate more complicated models.

C. Ship Classification Example Using the Bistatic RCS Model

An example of how data for comparison with such a model would be used for classification is shown in Fig. 7, for a ship represented by this monopole-pair model, traveling along the direction of the diamond head arrow pointing to the left and slightly downward. The RCS surface is the same as in Fig. 6, but seen from above in plan view with RCS in gray scale on the left. The illumination geometry is shown to the right for two bistatic sources, with the receiver site located below them. These transmit sites represent bistatic transmitters located at two islands of the Chesapeake Bay Bridge–Tunnel, VA, and the receive array site is at Point Henry at the mouth of the Chesapeake Bay. Site 1 is very close to the ship track direction as it approaches one of the two tunnels under the shipping channels. The three sets of lines represent scatter paths for three positions of the target moving from right to left, the diamond representing the ship's bow. The wave vectors for the two sites are seen to create bistatic angles just greater and just less than 90°, respectively, for each case, changing as the target progresses along its course. These three boat locations generate three samples of bistatic RCS versus frequency for each site, as indicated by the two sets of three vertical lines over the RCS plot to the left. The white lines represent the locus of RCS values measured for bistatic site 1 for the three positions, and the black lines represent site 2, as if one had continuous frequency coverage over the HF band. In practice, 30 discrete frequencies are more likely, so that discrete samples would occur along these lines to generate a matrix of frequency-bistatic angle samples for target classification. Both the maxima and deep minima would be used as the classifiers, with accuracy of classification increasing with greater number of aspect angle samples, and/or bistatic transmitter sources. The goal is to sample as many locations as possible in the frequency/aspect-angle domain. Of course algorithms to perform such classification would require development to achieve a robust classification tool.

In practice, a library of bistatic RCS values generated by a more accurate scattering model would be a more practical approach as a source of data comparison, or a comprehensive set of measurements for ships of particular interest. At a minimum, the lowest frequency RCS peak gives a general measure of the scale size of the target. Results by Headrick and Rachuba [20] show that a Naval combatant RCS extends through the HF band with no indication of a minimum value reached at 3 MHz, indicating vertical structures taller than a 3-MHz 25-m quarter wavelength monopole equivalent. They showed that the broadside RCS is generally 20 dB or more greater than the view along the stern, with no strong minima. Additionally, the stern view showed a series of resonant minima similar to that shown in the model presented here, suggesting that minima such as those shown in our model could be used as classifiers when the bulk broadside area illumination is avoided. To the authors' knowledge, no results of bistatic RCS have been published nor models generated for a specific ship superstructure in the unclassified literature.

D. Bistatic Operation and Transmit Power Requirements

The specific algorithms one would utilize using multifrequency radar data for classification in a multistatic mode remains to be developed. However, the results shown above produce a reasonable source of information for target classification. Bistatic illuminators might be sited either on land or open ocean platforms, floating or fixed sites. One advantage of bistatic illumination is that the transmit power requirements are reduced from that of monostatic illumination due to the difference in range-dependent losses of the radar equation (2). If one takes the logarithm of the equation, so that each term

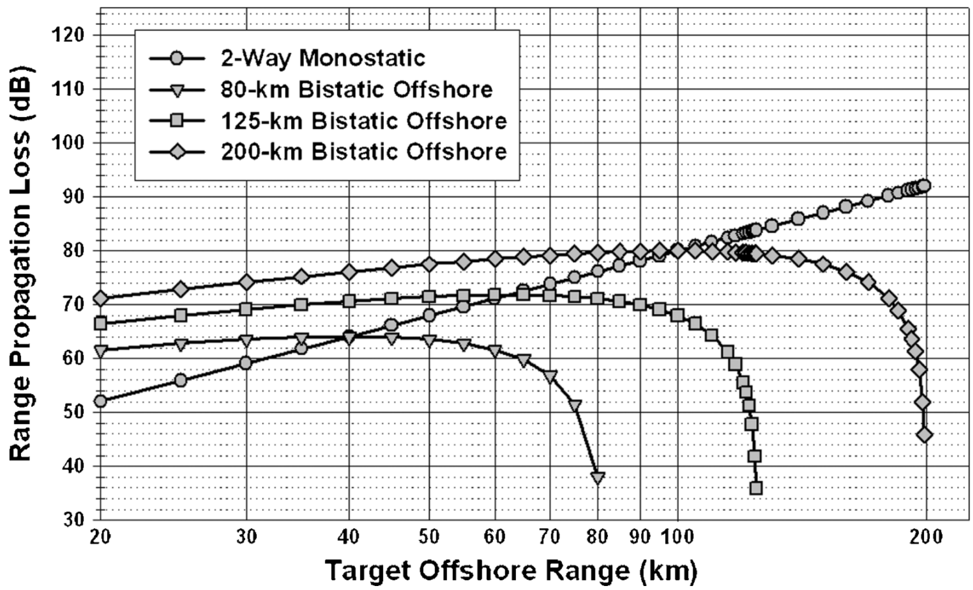

Fig. 8. Range loss comparisons for single-site monostatic and bistatic coverage using transmitters located at distances offshore 125 and 200 km show the gains achieved by bistatic illumination.

appears as a decibel value in a sum, then the total range loss for the two paths, illuminator to target, and target to receive array, can be written as loss terms

$$L_R = L_{R1} + L_{R2} = 20 \log_{10}(R_1 R_2). \tag{5}$$

For the case of a target coverage range of 20–124 km from the receive site, and bistatic transmitters placed at 80, 125, and 200 km offshore, the range loss comparison for the case of bistatic and monostatic illumination are shown in Fig. 8. The plots represent L_R for a target lying in a line between the bistatic illuminator and the receiver for each distance, and the monostatic loss is shown as the straight line on the log–log plot. The decibel difference in loss between the monostatic case and the bistatic cases for ranges beyond the crossover point for each bistatic curve represents an effective radar equation gain achieved for bistatic illumination, and allows the bistatic transmit antenna gain-transmit power product $G_T G_R P_T$ to be reduced accordingly for coverage at the longer ranges in each bistatic case over monostatic operation. Thus, while a rather robust transmit power and gain are required for monostatic coverage from the base receive site, the antennas and transmit power requirements can be modestly lower for operation from an open ocean platform due to shorter R_1 values. As less directive, antennas are expected to be more practical for floating platforms than one might be able to achieve on land. Instead of the LPA of Fig. 2, for example, a two-element tunable monopole pair array would probably be sufficient for a floating platform antenna. (Note that for bistatic operation, targets lying on the path directly between the bistatic transmitter and the receiver cannot be distinguished from the direct path signal, as they would both have the same time delay. Thus, the plots of Fig. 8 are for illustrative purpose only. The target must lie on the first bistatic range bin ellipse before it can be distinguished from the direct path signal, which we do not treat here.)

IV. Current Shear, Wind-Speed Retrieval, and Complex Deep Currents

Use of multiple frequencies allows one to map currents versus depth, as introduced previously. With sufficiently low radar frequencies and modest wind speed, one can measure currents below the wind-driven surface shear layer to identify other ambient currents not driven by the wind. Some results representing such a condition are presented next.

On August 27, 2003, we conducted a ship RCS experiment using 32 frequencies covering the HF band and a depth range equivalent to 0.4–4 m ($\sim$8% of Bragg resonant ocean wavelength, or 4% of radar wavelength [21]). Four-loop antenna elements identical to those shown in Fig. 2 were used in a linear receive array. These data were collected at a U.S. Navy field site off the coast of Point Loma, CA. The Doppler spectra were quite broad, indicating a complex current field near shore. Six spectra from a typical set are shown in Fig. 9 using a 64-s coherent integration for the Doppler analysis. Labels show radar frequency in megahertz, with predicted Bragg-line Doppler shift in hertz in the absence of currents. Targets between the Bragg lines are local ship target echoes.

Data files were collected for 512 s at a 2-Hz PRF, 1024 waveforms per file. This was repeated every 10 min for 75 min of boat runs. The unusual breadth of the Bragg lines offered an opportunity to submit the data to current measurement using direction-of-arrival (DOA) analysis, although the experiment was not designed to provide extensive time history as one would desire for a true current-mapping experiment.

These data were processed for DOA current analysis using a full data record, and a 1024-pt fast Fourier transform (FFT) to obtain maximum Doppler resolution. Four such consecutive files, as is required for four receive elements, were then submitted to proprietary direction-of-arrival analysis that is used to track target ships on boresight course to verify their identification from other ship traffic in the area. Here, the DOA spectral analysis focused on the Bragg-line components rather than

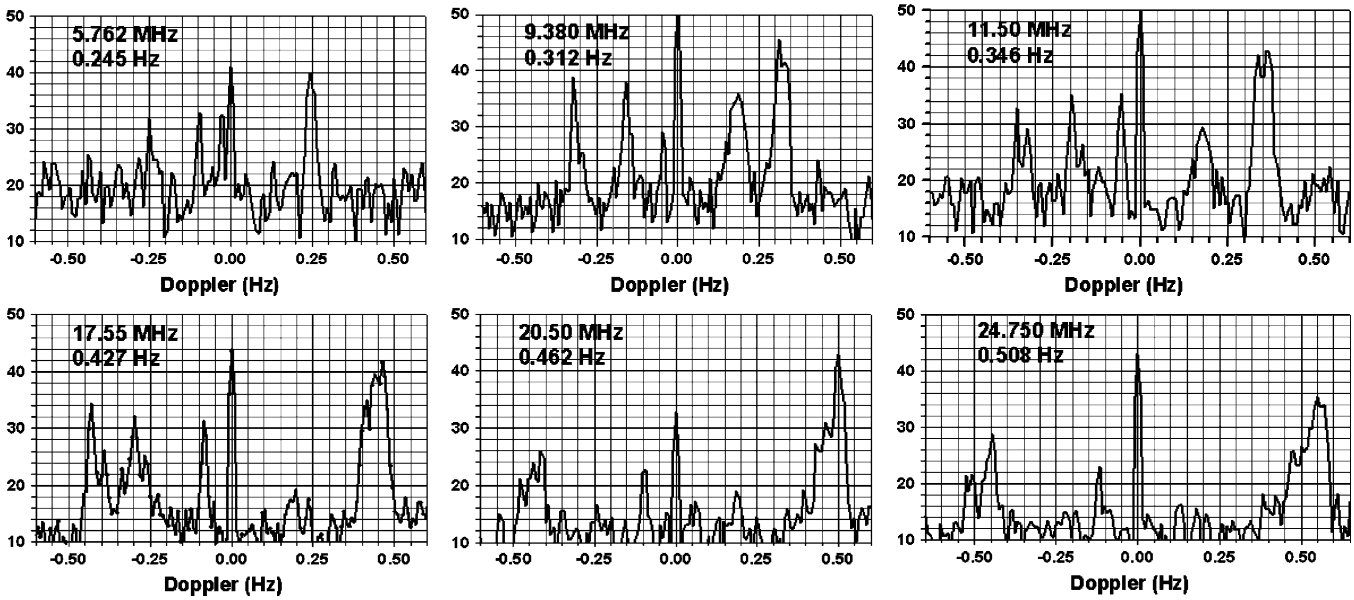

Fig. 9. Typical Doppler spectra with 64-s coherent integration for six of the 32 frequencies used, with radar frequency labeled in megahertz and Bragg-line Doppler shift in the absence of currents in hertz.

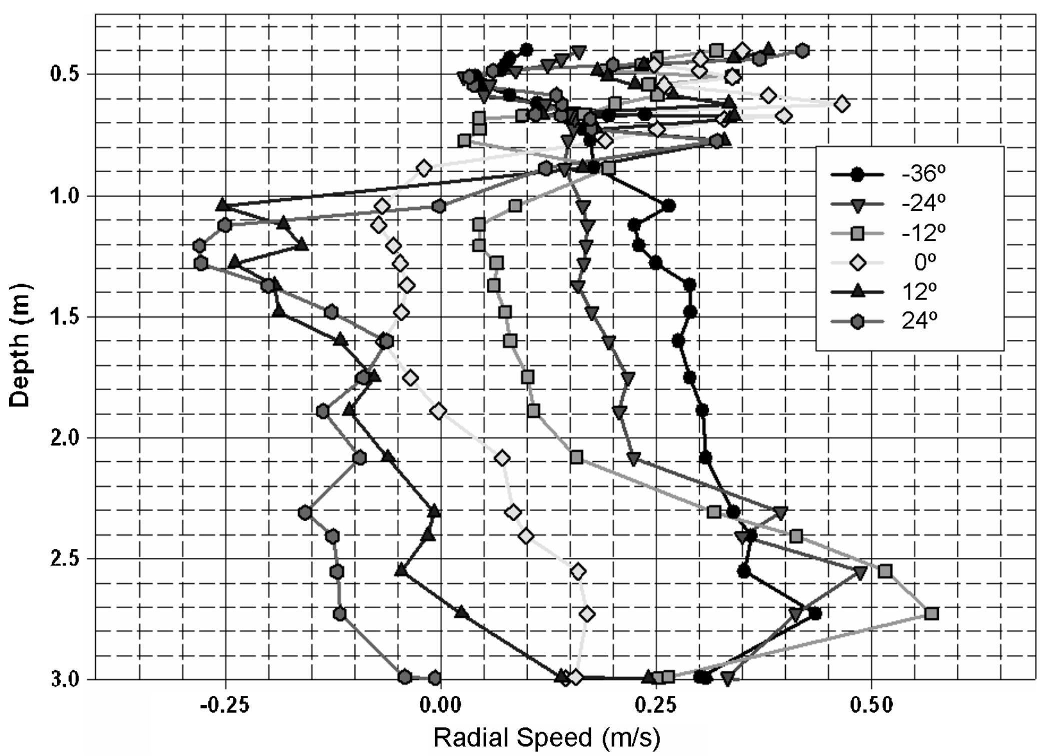

Fig. 10. Current plotted versus depth shows evidence of a southerly flow below 50-cm depth, as seen by the change in magnitude from one azimuth step to the next. This structure is masked in the top 50 cm by wind-driven current shear from a nearly orthogonal direction, suggesting that two flows can be present simultaneously, and a single-frequency radar cannot provide all the information one might desire.

the target echo, using all Bragg-line Doppler components with signal to noise ratio greater than 6 dB. The results of this analysis are summarized in Fig. 10. We have assigned the depths to be the 4% values of the radar wavelength, as is the convention of the HF radar community. The true effective depth is a value integrated over that depth, however, and the exact value is a subject of research that awaits accurate comparisons with sensors such as Doppler profilers. For the purpose of this paper, we simply adopt the HF community convention. Bragg-line data for the lowest frequencies were somewhat noisy, so a depth of 3 m was used as the deep-water cutoff in the display. Doppler shifts are plotted for interpolated 12° increments covering a total of 60° of coverage, with negative angle corresponding to bearing clockwise relative to 245° boresight.

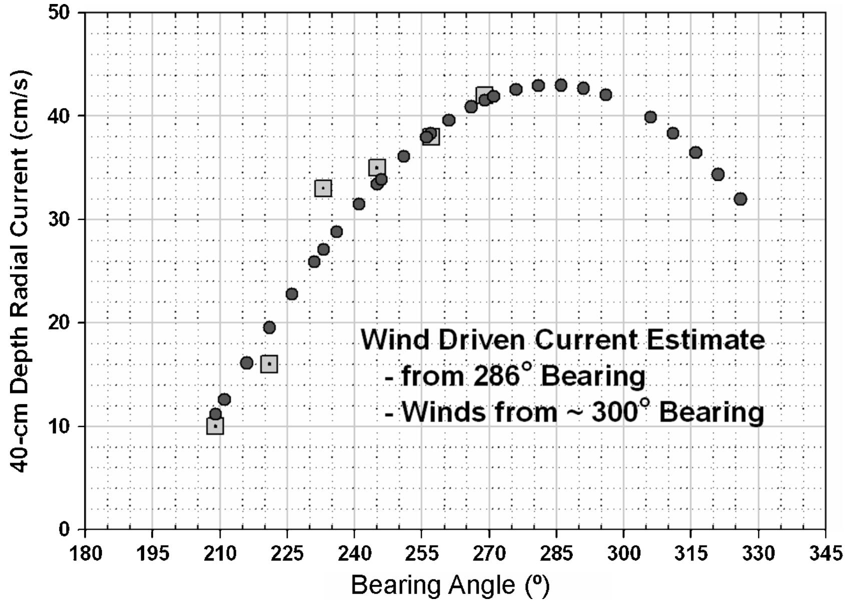

Fig. 11. Radial currents plotted for shallowest 40-cm depth versus true bearing compare well with a model projection of constant vector current flow from 286° bearing at 42 cm/s.

A. *Wind-Driven Surface Current and Current-Mapping Accuracy Issues*

Near the surface, one sees positive or approaching radial currents with $-36°$ as the minimum, indicating this bearing is closest to perpendicular to the upwind direction. The 24° azimuth shows maximum surface layer shift, indicating the direction nearest upwind. Fig. 11 shows the shallowest water radial current results plotted as squares versus actual radar bearing, and a best fit cosine function response centered on 286°. A cosine fit is what one would expect from radial components of a current of singular direction, as is presented by our observations in 12° steps. The data fit the curve quite well. Thus, the estimate of the surface current at 40-cm depth is 42 cm/s, from a direction of 286°.

According to the Ekman circulation theory, when wind and seas have reached equilibrium, the wind-driven current at the surface should run in a direction at 45° to the right of the wind direction in the northern hemisphere, and to the left in the southern hemisphere (see, for example, [22, Ch. 9]). For fresh winds, the surface current runs in the same direction of the wind. Thus, one expects the surface current to lie somewhere between 0 and 45° to the right of the local wind, depending on the level of equilibrium reached. The nearest National Weather Service National Data Buoy Center's buoys offshore California were considered as a source of accurate winds. The first two, #46047 and #46087, lie nearly due west, but at approximately 215 and 70 km away, respectively, and showed quite different speeds and directions. A third buoy, further up the coast near Santa Monica, #46025, was also addressed, and these data appeared similar to the other near-shore buoy, #46087, in speed and direction as shown in Fig. 12. The time is universal time, 7 h ahead of local Pacific daylight time (PDT). The experiment started at 12:30:00 P.M., or 19:30:00Z, 27.75 being 19:00:00Z. If one uses a local wind direction represented by #46047 far offshore, say from 300°, then the Ekman surface current should lie further to the right, and thus our measured direction should be greater than 300°, which is not the case. The winds closer to shore in both cases show a much weaker magnitude, and change direction of 90° over the 3-h period before the experiment. As a result of continuously turning wind field, wind wave equilibrium was probably not set up, so that the Ekman shift was probably not present. The measured 286° does agree with the local wind field, as it should for fresh winds, approximately in the same direction.

The current shear appears rather high, but this is due to the transition to a nonzero flow field at greater depth with rather large radial components, discussed later. Thus, the measured near-surface shear is not to be interpreted as a wind-driven log-layer because of the transition to the deeper flow values rather than zero. An application of how one might utilize such a log-layer current-shear measurement to estimate vector wind fields is discussed in Section IV-B. These results of the existence of deeper flow suggest that the accuracy of the log-layer can be influenced by the deeper flow. Alternatively, it suggests that the accuracy of radar measurement of deeper flow dynamics can be influenced by the surface wind-driven current layer. For example, if a single-frequency current-mapping radar were operating in the 12–20-MHz region, sampling the range of depths between 0.5 and 1 m where the transition occurs, neither the wind-driven surface layer nor the deeper water dynamics would be measured correctly. This points to the utility of multifrequency radar in capturing the flow field correctly.

B. *Log-Layer Current Structure for Wind-Speed Estimation*

Vesecky *et al.* [23], [24] and Meadows [25] have demonstrated that one can estimate the wind-speed vector from current-shear measurements by assuming continuity of the stress

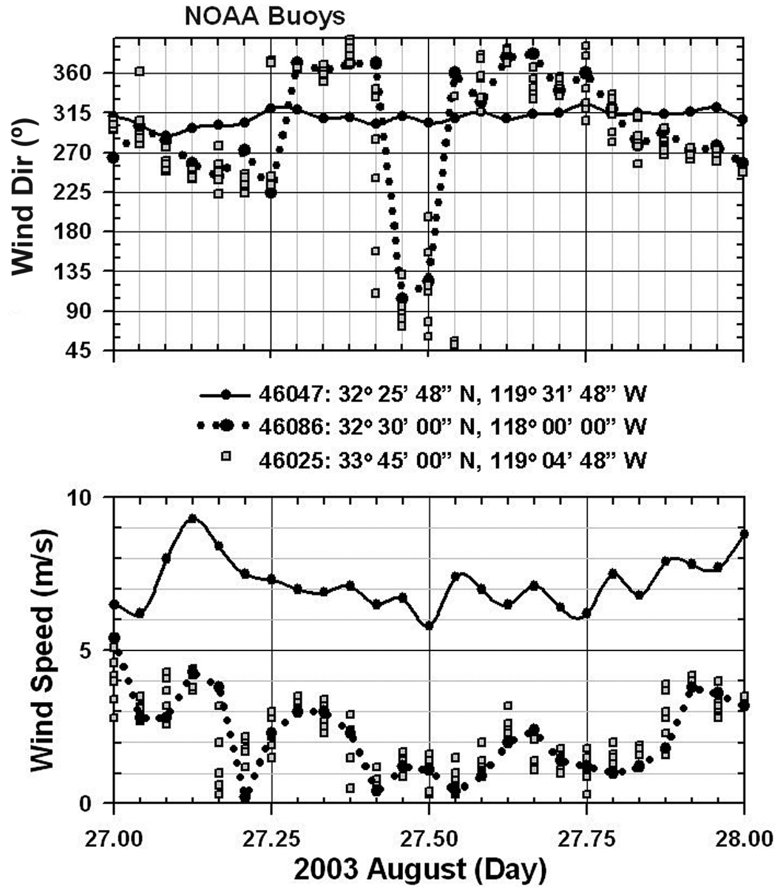

Fig. 12. Plots of wind speed and direction are shown for three National Data Buoy center (NDBC) buoys, the ones showing similar behavior lying closer to the coast than the third.

across the air–sea interface. The stress is proportional to the currents in the air (u_A^2) and water (u_w^2), as well as the densities of the two media (ρ_A and ρ_W), where the subscripts A and W refer to air and water, respectively

$$\rho_A u_A^2(Z=0) = \rho_w u_w^2(Z=0). \tag{6}$$

From this equation and Monin-Obukov theory, one can infer estimates of logarithmic profile of currents in the air from a measure of those in the water, and vice versa. Vesecky *et al.* [23], [24] used an instrumented buoy for surface truth winds in the center of a radar cell, derived wind-speed estimates from a derived wind profile, and in the comparison they found a standard error of 1 m/s, a bias of ~0.5 m/s, and a correlation of R^2~0.8. Their work demonstrates the utility of current shear to estimate wind fields that could not be gotten by other means as with the sampling density of HF radar. We cannot apply the method to the data presented here in a simple fashion, however, as the surface layer is influenced by the deeper flow as discussed previously, and is probably not representative of a true log-layer. Thus, some knowledge of the deeper ambient flow is necessary for estimation of accuracy of the algorithm fitting to a log-layer for such a reason.

C. Deep-Water Flow

The radial speed profile becomes complicated between about 50 cm and 1 m and is quite noisy. This is assumed to be due to the chaotic transition from the surface layer wind-driven current to a deeper flow field. At the rightmost bearing, 24°, the radial current is a maximum over most depths. Below 2 m, the relative radial magnitudes change sense, perhaps indicative of Ekman turning. As one considers bearings running to the left approaching boresight, the radials decrease in magnitude and approach zero between boresight and $-12°$. Using just a single range bin of constant radius, one might interpret these results as due to either the edge of a counterclockwise rotating eddy or flow due to a northerly current. Additional range bin information was used for better identification of the source of the flow.

Data were collected for four range bins spanning roughly 8 km; they were resampled to a latitude–longitude grid of 0.01° equal spacing, and are presented in Fig. 13. This provides a plan view of the current field for a single fixed 1.48-m depth from the set shown in the previous figure. The dot at each location represents the tail of the vector component, so that the current field has a northerly flow. Without a second set of radials from a second site, one cannot say definitively what type of flow is being sensed. This map could represent the edge of an offshore eddy of a few kilometers in diameter, or could be a slow turn in a north flowing current.

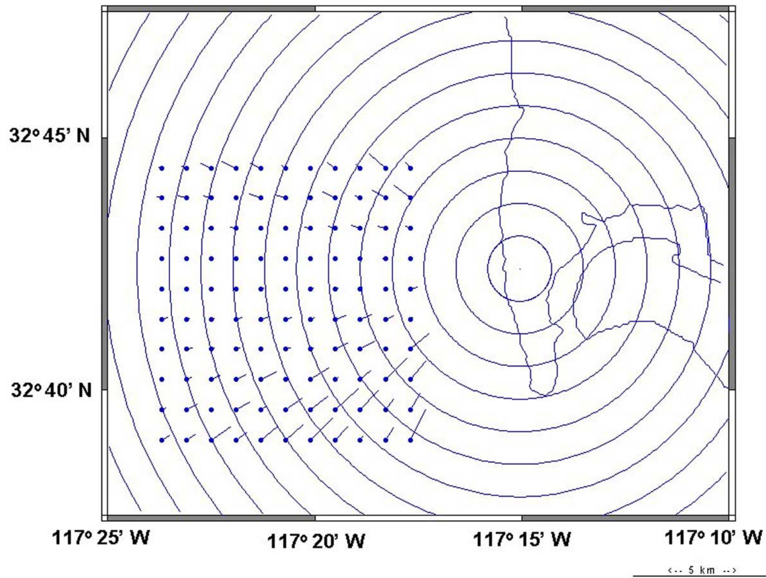

Fig. 13. Grid map of radial currents, derived from interpolation across four range bins and 12° azimuth steps for data from a depth of 1.48 m, mapping deeper water flow. The dot represents the tail of the arrow.

Both eddies and a northerly flow in this region have been reported using satellite visual and synthetic radar aperture imagery. The northerly flow is known as the southern California counter current, and eddies between 1 and 20 km diameter have been reported in this region using these data sources. We scanned the available imagery from NOAA websites for this period, but there were no data available for comparison on the day of the experiment. One might anticipate that the temperature image of warm or cold water eddies could be masked by a wind-driven mixed shear layer as shown by these HF radar data, and might make temperature identification impossible, even though the flow field is present in deeper water as shown here. Unfortunately, no such comparisons could be made due to the lack of visible imagery. These radar results suggest that the absence of an eddy in such satellite imagery does not rule out their presence, just their accurate surface expression. Independent HF radar current-shear maps provide a new research tool to test this hypothesis.

It was not the purpose of this work to conduct a scientific study of such flows, as insufficient data are available for such an effort. We only present this cursory analysis to demonstrate the utility of multifrequency HF radar and its potential application to the oceanographic community, as well as raise some questions about data interpretation from single-frequency radars. This discussion of the presence of dual-process flow fields, and the transition between them, raises questions about the ability of a single-frequency radar to capture an accurate representation of the complete flow, particularly in the presence of a strong wind field.

D. Volumetric Current Mapping Using Multifrequency Radar and Projection Models

Shen and Evans [26], [27] have demonstrated a method to utilize a matrix map time series of near-surface current shear, in the latitude–longitude format of Fig. 13, to develop estimates at each location of the current profile to the bottom in depths of 50 m or less. They develop a linearization of the equations of motion of the fluid in space and time, and apply it to the measurements of the near-surface current shear (or to a map of surface currents with an estimate of the shear based on the local wind field). The result of this analysis is what they term as a "projection" of the currents to the bottom. Currently, there is no method by which volumetric estimates of the current field can be obtained from near-surface data, or from a realistic number of *in situ* sensors. This approach emphasizes the utility of multifrequency radar measurements of near-surface current shear and the promise this application holds for the future.

V. Summary

We have discussed a new HF radar that we have developed that is based on a multifrequency design. It can be deployed in either a standard monostatic pair format, or multistatic with a single receive site that provides all signal reception and signal processing with bistatic transmit sites that require less coastline space. Control of the bistatic transmitter sites is achieved by radio network link, and the master site is in full control of all radar assets. The system can be deployed either as a long array, 8, 16, or 32 elements using beamforming processing, or as a small four-element receive array using direction of arrival analysis. We have operated the system using 32 frequencies for U.S. Navy RCS applications, but a system could be deployed for ocean current shear mapping using as little as four to eight frequencies to derive a suitable estimate of current shear. The radar is based on a fully digital design, and aside from amplifier units on transmit and receive, there are no radio frequency components within the system. This eliminates many issues of calibration and temperature variation usually associated with RF components, some local noise interference issues, and substantially reduces the cost of assembly of HF radar systems.

Examples of multifrequency RCS measurements conducted by the first author of this paper and others in the 1970s were presented, showing characteristic RCS peaks and nulls that could be used as a classification tool. A simple model of two monopoles of different heights, representing a pair of masts or long antennas, was used to demonstrate how RCS peaks and nulls can occur due to constructive and destructive interference between the echoes from each element. These peaks and nulls were shown to be sensitive to bistatic illumination angle. With a library of bistatic RCS measured values for a series of ship classes, or a quantitative scattering model providing such a library, classification of ship targets could be achieved using a multifrequency HF radar operating across the HF band. Examples of the use of bistatic transmitters offshore indicate that propagation loss can be minimized compared to monostatic operation only for longer ranges, providing multiple bistatic angles to enhance target classification.

Surface current fields were derived from a set of measurements using 32 radar frequencies spanning the HF band. These showed a surface layer wind-driven current at 40-cm depth consistent with a flow of 42 cm/s from a 210° bearing off the west coast of southern California. At depths below 1 m, the current field indicated the presence flow with a northerly component and of larger magnitude than the wind-driven surface current. This suggests that wind-driven shear may mask deeper water flows if a single HF radar is used to map currents using the upper HF band. It also suggests that a single-frequency HF radar may provide incorrect results if the sampling depth occurs in the transition region between the wind-driven layer and deeper flow patterns. From multi-frequency current-shear fields, others have shown that wind field maps can be derived. In similar fashion, time sequences of current-shear maps can be used for water depths less than ∼50 m to extract volumetric current fields from the surface to the bottom. The use of multiple frequencies to such applications expands current capabilities and tools available to the oceanographic community.[2]

ACKNOWLEDGMENT

The authors would like to thank the reviewers for valuable suggestions that greatly improved the paper, and allowed them to correct an error in our original analysis due to the ubiquitous sign error.

REFERENCES

[1] J. M. Headrick and M. Skolnik, "Over-the-horizon radar in the HF band," *Proc. IEEE*, vol. 62, no. 6, pp. 664–673, Jun. 1974.

[2] E. D. R. Shearman*, Modern Radar Techniques*, M. J. B. Scanlan, Ed. London, U.K.: Collins Technical Books, 1987, ch. 5.

[3] A. E. Long and D. B. Trizna, "Mapping of North Atlantic winds by HF radar backscatter interpretation," *IEEE Trans. Antennas Propagat.*, vol. AP-21, no. 5, pp. 680–685, Sep. 1973.

[2]We continue to test radar improvements and modifications at our USACE FRF field site, and updates on progress and other publications and reference material can be found at the ISR website at www.isr-sensing.com

[4] J. L. Ahearn, S.R. Curley, J. M. Headrick, and D. B. Trizna, "Tests of remote skywave measurements of ocean surface conditions," *Proc. IEEE*, vol. 62, no. 6, pp. 681–687, Jun. 1974.

[5] R. H. Stewart and J. R. Barnum, "Radio measurements of oceanic winds at long ranges: An evaluation," *Radio Sci.*, vol. 10, pp. 853–857, 1975.

[6] J. W. Maresca, Jr. and J. R. Barnum, "Measurement of oceanic wind speed from HF sea scatter by skywave radar," *IEEE Trans. Antennas Propagat.*, vol. 25, no. 1, pp. 132–136, Jan. 1977.

[7] J. R. Barnum, J. W. Maresca, Jr., and S. M. Serebreny, "High-resolution mapping of oceanic wind fields with skywave radar," *IEEE Trans. Antennas Propagat.*, vol. AP-25, no. 1, pp. 128–132, Jan. 1977.

[8] D. E. Barrick, J. M. Headrick, R. W. Bogle, and D. D. Crombie, "Sea backscatter at HF: Interpretation and utilization of the echo," *Proc. IEEE*, vol. 62, no. 6, pp. 673–680, Jun. 1974.

[9] C. C. Teague, "Multifrequency HF radar observations of currents and current shears," *IEEE J. Ocean. Eng.*, vol. OE-11, no. 2, pp. 258–269, Apr. 1986.

[10] D. M. Fernandez, J. F. Vesecky, and C. C. Teague, "Measurements of upper ocean surface current shear with high-frequency radar," *J. Geophys. Res.*, vol. 101, pp. 28,615–28,625, 1996.

[11] D. B. Trizna, R. W. Bogle, J. C. Moore, and C. M. Moore, "Observation by HF radar of the phillips resonance mechanism for generation of wind waves," *J. Geophys. Res.*, vol. 85, pp. 4946–4956, 1980.

[12] J. W. Maresc Jr., T. M. Georges, C. T. Carlson, and J. P. Riley, "Two tests of real-time ocean wave-height mapping with HF skywave radar," *IEEE J. Ocean. Eng.*, vol. OE-11, no. 2, pp. 180–186, Apr. 1986.

[13] T. M. Georges, J. W. Maresca Jr., J. P. Riley, and C. T. Carlson, "Real-time sea-state surveillance with skywave radar," *IEEE J. Ocean. Eng.*, vol. OE-8, no. 2, pp. 97–103, Apr. 1983.

[14] B. J. Lipa and D. E. Barrick, "Tidal and storm-surge measurements with single-site CODAR," *IEEE J. Ocean. Eng.*, vol. OE-11, no. 2, pp. 241–245, Apr. 1986.

[15] B. J. Lipa, D. E. Barrick, J. Isaacson, and P. M. Lilleboe, "CODAR wave measurements from a North Sea semisubmersible," *IEEE J. Ocean. Eng.*, vol. OE-15, no. 2, pp. 119–125, Apr. 1990.

[16] C. T. Calvin, J. F. Vesecky, and Z. R. Hallock, "A comparison of multi-frequency HF radar and ADCP measurements of near-surface currents during COPE-3," *IEEE J. Ocean. Eng.*, vol. 26, no. 3, pp. 399–405, Jul. 2001.

[17] J. F. Vesecky, J. Drake, K. Laws, F. Ludwig, C. Teague, and L. Meadows, "Mapping vector, surface winds over the ocean with multi-frequency HF radar and non-linear retrieval," in *Proc. Int. Geosci. Remote Sens. Symp.*, Seoul, Korea, Jul. 25–29, 2005.

[18] R. W. Bogle and D. B. Trizna, "Small boat HF radar cross sections" Naval Research Lab., Washington, DC, Memorandum Rep. 3322, Jul. 1976.

[19] M. I. Skolnik*, Introduction to Radar Systems*, 3rd ed. New York: McGraw-Hill, 2001.

[20] J. M. Headrick and M. E. Rachuba, "High frequency band radar cross section measurement of ships" Naval Research Lab., Washington, DC, Memorandum Rep. 5309-98-8173, Feb. 1998.

[21] R. H Stewart and J. W. Joy, "HF radio measurements of ocean surface currents," *Deep Sea Res.*, vol. 21, pp. 1039–1049, 1974.

[22] R. H. Stewart, "Introduction to physical oceanography, open source textbook" Texas A&M Univ., College Station, TX [Online]. Available: http://oceanworld.tamu.edu/resources/ocng_textbook/contents.html

[23] J. F. Vesecky, J. Drake, C. C. Teague, F. L. Ludwig, K. Davidson, and J. Paduan, "Measurement of wind speed and direction using multi-frequency HF radar," in *Proc. IEEE Int. Geosci. Remote Sens. Symp.*, Jun. 2002, pp. 1899–1901.

[24] J.F. Vesecky, L. A. Meadows, Y. M. Fernandez, C. C. Teague, J. M. Daida, J. R. Paduan, R. del Gado, and P. E. Hansen, "HF radar observations of wind-current relationships at the air-sea boundary," in *Proc. IEEE Int. Geosc. Remote Sens. Symp.*, June 1999, vol. II, pp. BBC02.11.1–BBC02.11.3.

[25] L. A. Meadows, "High frequency radar measurements of friction layer in the marine boundary layer," Ph.D. dissertation, Dept. Naval Architecture Marine Eng., Univ. Michigan, An Arbor, 2002.

[26] C. Y. Shen and T. E. Evans, "Dynamically constrained projection for subsurface current velocity," *J. Geophys. Res.*, vol. 107, pp. 24-1–24-13, 2002.

[27] C. Y. Shen and T. E. Evans, "Surface to sub-surface velocity projection for shallow water currents," *J. Geophys. Res.*, vol. 106, pp. 6973–6984, 2001.

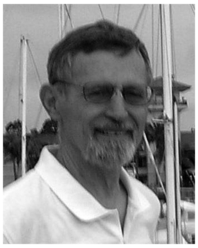

Dennis Trizna (M'74–SM'03) received the B.S. degree in physics from Benedictine University, Lisle, IL, in 1963 and the Ph.D. degree in physics from Iowa State University, Ames, in 1970.

He joined the Naval Research Laboratory (NRL) Radar Division, Washington, DC, in 1970, beginning his career in the area of OTH HF radar, with work in remote sensing of winds at sea using the NRL MADRE radar. In addition to other HF radar studies of interest to the U.S. Navy, he has published in the areas of microwave propagation and radar sea scatter, and has worked on the development of coherent microwave and marine radars to measure sea surface parameters. He served as a Scientific Officer at the U.S. Office of Naval Research for the Remote Sensing Program for eight years, in tandem with his duties as Head of the Small Scale Ocean Surface Processes Section at NRL. In this joint role, he has managed the development of two new radar systems: an ultrawideband multichannel SAR for use on light aircraft, and a multifrequency HF radar for the measurement of ocean current shear. In 2001, he retired from government service, and established Imaging Science Research (ISR), Incorporated, Burke, VA, business dedicated to development of radar technologies for coastal and ocean research.

Dr. Trizna is a Senior Member of the IEEE Geoscience and Remote Sensing Society, the IEEE Ocean Engineering Society, the IEEE Antennas and Propagation Society, the American Geophysical Union, and the American Physical Society.

Lillian (Xialon) Xu received the B.S. degree in biomedical electrical engineering (with highest honors) in 1986 and the M.S. degree in electrical engineering in 1989, both from Xian Jiaotong University, Xian, China and the Ph.D. degree from the Department of Electrical and Computer Engineering, George Mason University, Fairfax, VA, in 2002, under Prof. Harry Van Trees, with a dissertation on application of direction of arrival methods to azimuthal direction estimation of ship targets using microwave radar arrays.

She joined Imaging Science Research (ISR), Incorporated, Burke, VA, in 2004, as a part-time Research Associate.